

Metallurgical Investigation into Ductility Dip Cracking in Ni-Based Alloys: Part I

Quantifying cracking susceptibility during the first thermal cycle using the Gleeble® hot ductility test

BY F. F. NOECKER II AND J. N. DUPONT

ABSTRACT

Alloy 690 (A690) is a Ni-Cr-Fe alloy with excellent resistance to general corrosion, localized corrosion, and stress corrosion cracking. However, the companion filler metal for A690, Filler Metal 52 (FM52), has been shown by several researchers to be susceptible to ductility dip cracking (DDC), which limits its widespread use in joining applications. The Gleeble® hot ductility test was used to evaluate the DDC susceptibility of wrought Alloy 600 (A600) and A690, along with their companion filler metals, Filler Metal 82H (FM82H) and FM52, throughout the heating and cooling portions of a simulated weld reheat thermal cycle. Both macroscopic mechanical measures (ductility and ultimate tensile strength (UTS)) and microscopic measures (normalized crack length) of DDC were quantified and compared. The greatest resistance to DDC was observed in A600 and A690 during heating where no DDC cracks formed even when the samples were fractured. Both A690 and FM52 were found to form an intermediate on-cooling dip in ductility and UTS, which corresponded to an increase in DDC crack length normalized per grain boundary length. Ductility dip cracks were preferentially oriented at a 45-deg angle to the tensile axis and were of a wedge type appearance, both of which are indicative of grain boundary sliding (GBS). The hot ductility and cracking resistance of FM82H remained high throughout the entire thermal cycle. DDC susceptibility in both FM52 and FM82H decreased when the thermal cycle was modified to promote coarsening/precipitation of intergranular carbides. These intergranular carbides appear to decrease DDC susceptibility by limiting grain boundary sliding. A more detailed treatment of microstructural and microchemical evolution during the weld thermal cycle and their influence on the mechanism(s) of DDC is discussed in the Part II companion paper (Ref. 1).

Introduction

Nuclear energy provides for nearly 15% of the world commercial electrical power production with France, Sweden, and the Ukraine deriving nearly 50% or more of their electrical power from nuclear energy (Ref. 2). Nuclear reactors produce 20% of electrical power in the United States (Ref. 2), and power nearly 100% of aircraft carriers and submarines in the U. S. Navy's fleet (Ref. 3). For their safe and reliable operation, nuclear reactors require materials that are highly corrosion resistant, particularly to intergranular stress corrosion cracking (IGSCC).

For more than 40 years, Ni-Cr-Fe alloys such as A600 have been used for several key components in nuclear reactors due to their corrosion resistance. However, A600 has been found to be particularly susceptible to IGSCC in certain applications and environments (Refs. 4, 5). The replacement alloy for A600 is A690, which has excellent resistance to general corrosion, localized corrosion, and IGSCC in a wide range of environments (Ref. 6). Alloy 690 has been replacing A600 in United States commercial power plants since 1988 (Ref. 7). However, the companion filler metal for A690, FM52, has been shown by several researchers to be susceptible to ductility dip cracking (DDC), which limits its widespread use. This has resulted in the undesirable situation where FM82H, the companion weld filler metal to A600, may be used to join A690 due to its weldability despite its susceptibility to IGSCC in applications where the improved corrosion resistance

of FM52 is desired, thereby compromising the service life of the component for weldability.

There are several key characteristics of DDC. First, as the name "ductility dip" implies, there is significant reduction in ductility that occurs at intermediate temperature, corresponding to approximately 0.5 to 0.8 homologous temperature (T_m) of the alloy. Secondly, DDC is an intergranular form of cracking. Third, there are no liquid films associated with DDC. Unlike other common forms of weld cracking, such as liquation and solidification cracking, DDC is a solid-state phenomenon.

A substantial amount of research has recently been performed on ductility dip cracking in these alloys (Refs. 8–19) and in other austenitic alloys (Refs. 20–27); however, the mechanism of DDC is not fully understood and may differ among different alloys. Several hypotheses have been proposed to include grain boundary sliding (Refs. 13, 16, 25–28), intergranular impurity element embrittlement (P, S, and H) (Refs. 9–11, 16, 20, 21, 23), and intergranular second phase precipitation (Refs. 11, 19, 27, 29).

Multiple techniques have been used to evaluate DDC susceptibility. These include multipass welds, and Vareststraint and Gleeble®-based testing. Multipass welds and Vareststraint tests have several limitations that make them less than ideal for a carefully controlled investigation into the mechanism of DDC. In both techniques liquid films can form, which can confound the interpretation of cracking results. Furthermore, many multipass weld tests utilize in excess of 100 weld passes. Each region of a multipass weldment experiences a different thermal history, which will result in different microstructures and potentially different DDC susceptibility levels throughout the

KEYWORDS

Alloy 690 (A690)
Alloy 600 (A600)
Filler Metal 52 (FM52)
Filler Metal 82H (FM82H)
Ductility Dip Cracking (DDC)
Ultimate Tensile Strength (UTS)
Grain Boundary Sliding (GBS)

F. F. NOECKER II (ffn2us@yahoo.com), formerly a research assistant, Department of Materials Science and Engineering, Lehigh University, Bethlehem, Pa., is currently a materials specialist, Exxon-Mobil, Upstream Development Co., Houston, Tex. J. N. DUPONT is a professor, Department of Materials Science and Engineering, Lehigh University, Bethlehem, Pa.

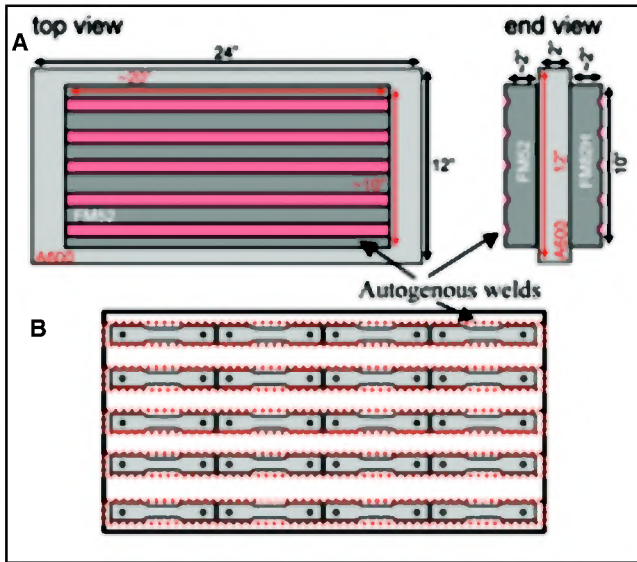


Fig. 1 — Preparation of FM52 and FM82H as-solidified weld metal samples. A — FM52 and FM82H were deposited onto A600, then autogenous welds were made onto weld pad buildup. B — layer of autogenous welds sectioned from weld pad, then dogbone specimens sectioned from this layer. All dimensions in inches.

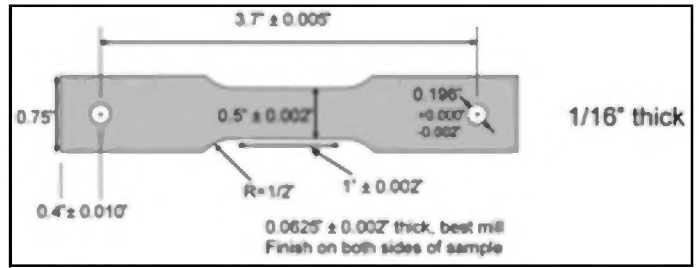


Fig. 2 — Schematic of the Gleeble® specimen.

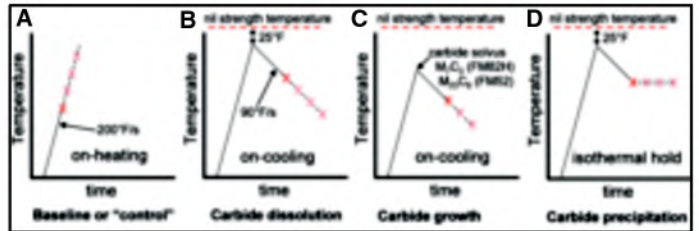


Fig. 3 — Schema for Gleeble® weld reheat thermal cycle showing samples that were hot ductility tested both on-heating and on-cooling.

sample. Thus, it is extremely difficult to confidently identify causes of DDC given such complex thermal mechanical history. Lastly, it is difficult, if not impossible, to capture and study the elevated temperature microstructure and microchemistry existent at grain boundaries using these tests because of their inherent difficulty of rapidly quenching the weld at precise time/temperatures in the weld thermal cycle. Because DDC forms intergranularly, understanding the microchemical and microstructural evolution at the grain boundaries during a weld reheat thermal cycle is key to furthering the mechanistic understanding of DDC.

There are several advantages to using a Gleeble®-based test to investigate the metallurgical mechanism(s) that cause DDC. First and foremost, the thermal profile can be carefully controlled. Proper control of peak temperature in the Gleeble® eliminates the formation of liquid films and the aforementioned problems associated with them. The precise control over the weld thermal cycle also enables the weld mechanical properties to be quantified at precise temperatures/times throughout the weld reheat thermal cycle. Lastly, a Gleeble®-based test produces a

large volume of material that has experienced the same thermal history, particularly compared to fusion-based welding tests where the temperature gradients can be very high (Ref. 30). The larger volume of material greatly aids the identification and characterization of detrimental microstructures, and/or segregants that may form at temperatures/times in the weld reheat thermal cycle.

The vast majority of previous studies that used hot tension/Gleeble®-based tests to investigate DDC have only evaluated cracking susceptibility while the material is being heated (on-heating), or cooled (on-cooling), but not both. Since the material in any heat-affected zone (HAZ) experiences both heating and cooling, this investigation will evaluate both the on-heating and on-cooling DDC susceptibility.

Although Gleeble®-based testing has many advantages, little is known about how the macroscopic mechanical measurements of an alloy's behavior, like ductility and ultimate tensile strength, correlate to DDC susceptibility. Furthermore, some hot tension/Gleeble®-based work has shown that DDC susceptibility has a stroke rate dependence (Refs. 8, 24, 31);

therefore, a suitable stroke rate for DDC testing of the alloys of interest in this investigation must be identified.

The overall objectives of this work were threefold. The first objective was to identify the temperature regime in which the alloys under investigation are metallurgically most susceptible to form DDC cracks. This was accomplished by using a carefully controlled thermal cycle representative of typical multipass welding to determine the DDC susceptibility during the first weld thermal cycle using the Gleeble® hot ductility test. Toward this end a suitable stroke rate must be identified that will reliably reproduce DDC in alloys that are known to be susceptible based on previous welding experience. Second, the macroscopic properties of the reheated metal will be compared to the microscopic formation of ductility dip cracks. Although the Gleeble® hot ductility test has been used in the past to evaluate DDC susceptibility of alloys, there has yet to be a study that identifies the relationship between DDC formation, which occurs on the microscopic scale, and its effects on macroscopic mechanical properties (ductility, strength). The final objective is to investigate the effects of peak temperature and isothermal hold, both of which should affect

Table 1 — Alloy Compositions in Weight-Percent

	Ni	Cr	Fe	C	Mn	S	Si	Cu	Nb	Ti	Al	Ti+Al	P	Mo	Other
A600	75.67	14.7	8.22	0.079	0.36	0.001	0.25	0.01	—	—	—	—	—	—	—
FM82H	71.52	20.38	2.26	0.049	2.99	0.002	0.06	0.01	2.28	0.3	0.04	0.34	0.002	—	<0.5
A690	60.75	29.28	9.12	0.025	0.17	<0.001	0.08	0.01	<0.01	0.3	0.22	0.52	0.005	0.01	—
FM52	59.12	29.13	10.08	0.027	0.25	<0.001	0.13	0.01	<0.01	0.51	0.71	1.22	0.003	0.01	<0.5

the volume fraction of intergranular precipitates, on DDC susceptibility. A more detailed treatment of microstructural and microchemical evolution during the first thermal cycle, and how that relates to the mechanism(s) of DDC, are discussed in the Part II companion paper (Ref. 1).

Experimental Procedure

Sample Preparation

Four alloys were investigated as part of this work: A600 (UNS: N06600) and A690 (UNS: N06690) along with their respective companion filler metals FM82H (AWS: ERNiCr-3) and FM52 (AWS: ERNiCrFe-7). Nominal compositions for each alloy are given in Table 1. A600 and A690 form the base metal material in multipass weldments; therefore, they were tested in the wrought condition as part of this work. Alloy 600 and A690 Gleeble® specimens were fabricated directly from 1-in.- (25.4-mm-) thick plate with the width, length, and thickness of the specimens corresponding to the thickness, longitudinal, and width directions of the plate, respectively. Select A690 specimens were also tested in the as-solidified condition.

Unlike A600 and A690, the starting material condition of FM52 and FM82H in the weldment is as-solidified. To best study the DDC susceptibility of the weld metals, they should be in the same condition as they are in a multipass weld before they experience the first thermal cycle. This requires FM52 and FM82H be tested in the as-solidified condition as part of this work. FM52 and FM82H only come in weld wire form, therefore the weld metal was first deposited by successive beads on a plate of A600 to form a weld pad buildup as shown in Fig. 1A. The corresponding welding parameters are given in Table 2. A total of 18 layers of weld deposits were made for each alloy (FM82H and FM52), each approximately 1/8 in. (3.2 mm) thick. To ensure that weld metal dilution did not affect the weld metal chemistry in the final Gleeble® samples, all of the samples were made from the top 0.75 in. (19 mm) or 7 layers of weld pad buildup. Weld metal dilution from the A600 base metal did not play a role in the chemistry of the final weld metal samples due to the large number of weld passes between the base metal and the samples, and the relative compositional similarity in the three Ni-Cr-Fe alloys: FM82H, FM52, and A600.

Autogenous welds were then made on this weld pad buildup to produce regions of as-solidified weld metal that corresponded to the longitudinal axis of the tensile specimens that were subsequently tested in the Gleeble® — Fig. 1A. It was important to ensure this as-solidified material did not see a significant reheat during a subsequent au-

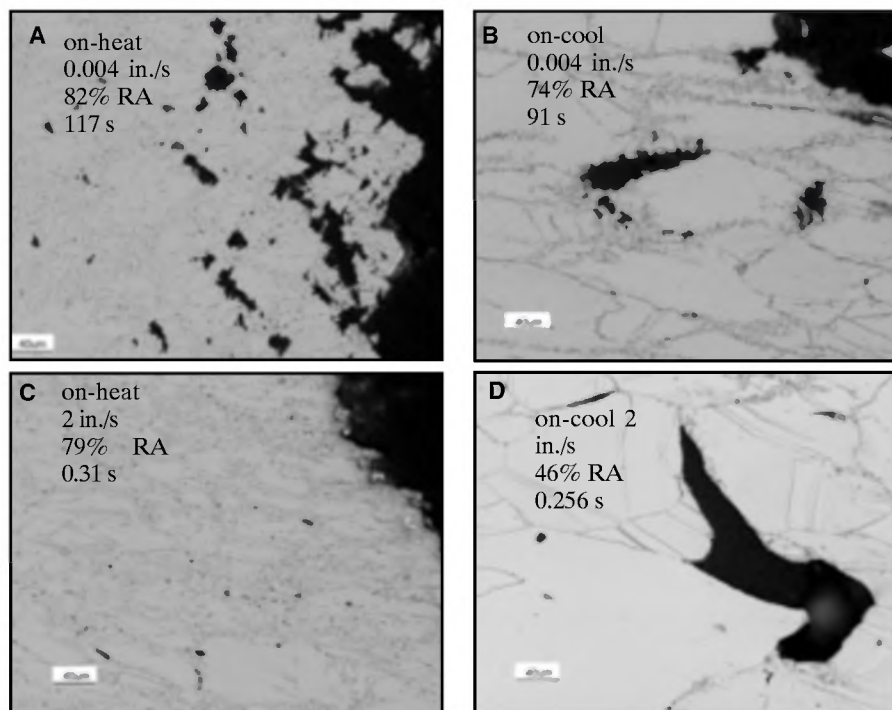


Fig. 4 — LOM photomicrographs of A690 Gleeble® hot ductility specimen tested at 1600°F using 0.004 in./s stroke rate (A and B) and 2 in./s stroke rate (C and D). A and C were tested on-heating while B and D were tested on-cooling. %RA and time under strain, in seconds, are provided on each micrograph.

togenous weld pass for it to be considered “as-solidified.” Therefore, sufficient spacing had to be maintained between the autogenous welds to prevent microstructural changes in a previously deposited pass. Time-temperature transformation (TTT) diagrams were used to determine the maximum temperature the previously deposited weld pass could experience during the brief time interval typical of welding without changing the precipitate microstructure. Since TTT diagrams for FM52 and FM82H are not available in the literature, they were calculated based on the nominal composition of each alloy using JMatPro 3.0 (Refs. 32, 33). It was found that a transient peak temperature of 575°F (302°C) should not cause significant changes in precipitate volume fraction. Preliminary work showed that a 2-in. (50.8-mm) separation between auto-

genous weld centerlines would ensure that the maximum temperature in a previous autogenous weld pass never exceeded 575°F. Welding parameters for the autogenous welds are given in Table 2. These same welding conditions were also used to make select A690 as-solidified specimens.

A thin layer (~1/8 in. (1.6 mm) thick) of the weld pad containing autogenous welds was then sectioned from the weld pad buildup using wire electrical discharge machining (EDM). Gleeble® hot ductility test specimens were sectioned from this layer using waterjet cutting as shown in Fig. 1B. The final tensile specimen specifications are shown in Fig. 2. For the FM82H and FM52 specimens, the entire sample was comprised of as-solidified weld metal. The same design was also used with the A600 and A690 test specimens,

Table 2 — Weld Pad and Autogenous Weld Parameters

Parameter	Weld pad	Autogenous welds
Shielding gas/flow (ft ³ /h)	Ar / 43	He / 160
Electrode	5/32 in. diam., 2% Ceriated-Tungsten	5/32 in. diam., 2% Ceriated-Tungsten
Electrode included angle	50 deg	180 deg
Current (A)	310	247
Potential (V)	12	15.5
Travel speed: (in./min)	6.7	3.4
Magnetic oscillation: (cycles/min)	100	100
Hot Wire		n/a
Diameter (in.)	0.045	n/a
Current (A)	80	n/a
Potential (V)	6.2	n/a
Feed rate (in./min)	170	n/a

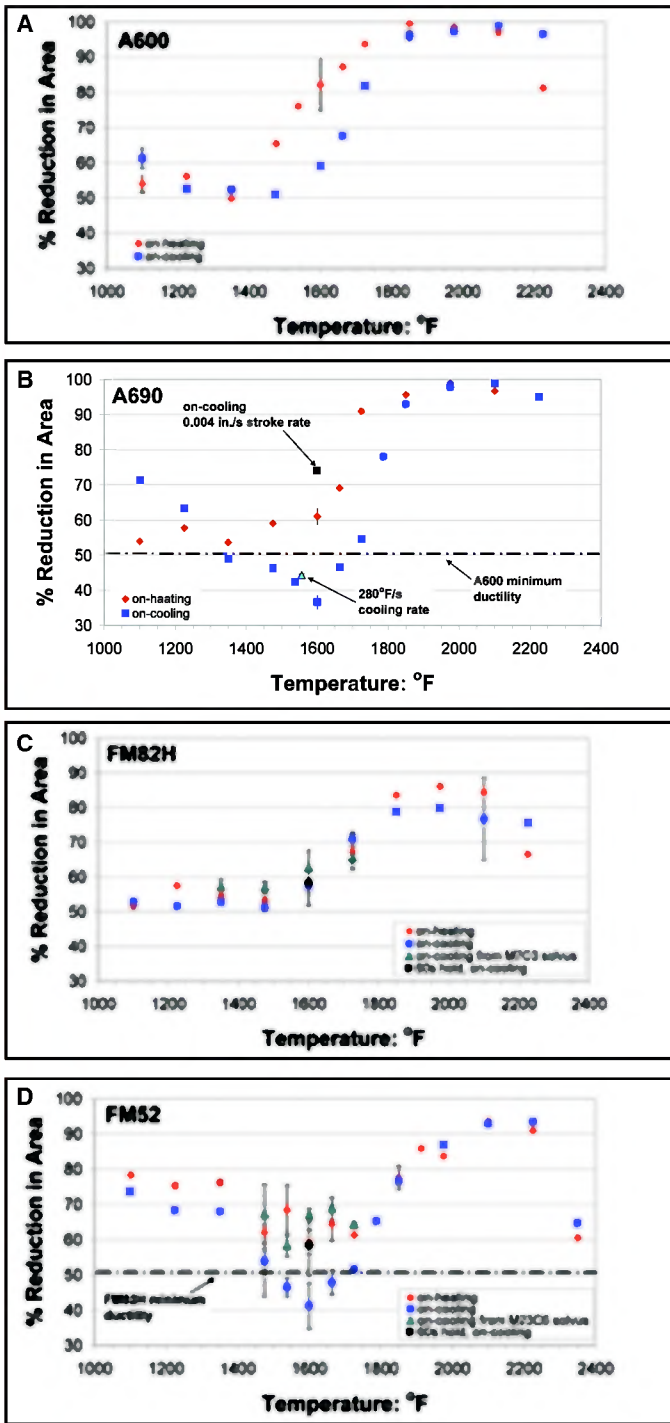


Fig. 5 — On-heating and on-cooling hot ductility curves for the following: A — A600; B — A690; C — FM82H; and D — FM52. FM82H and FM52 hot ductility curves also include on-cooling data from their respective carbide solvus temperatures.

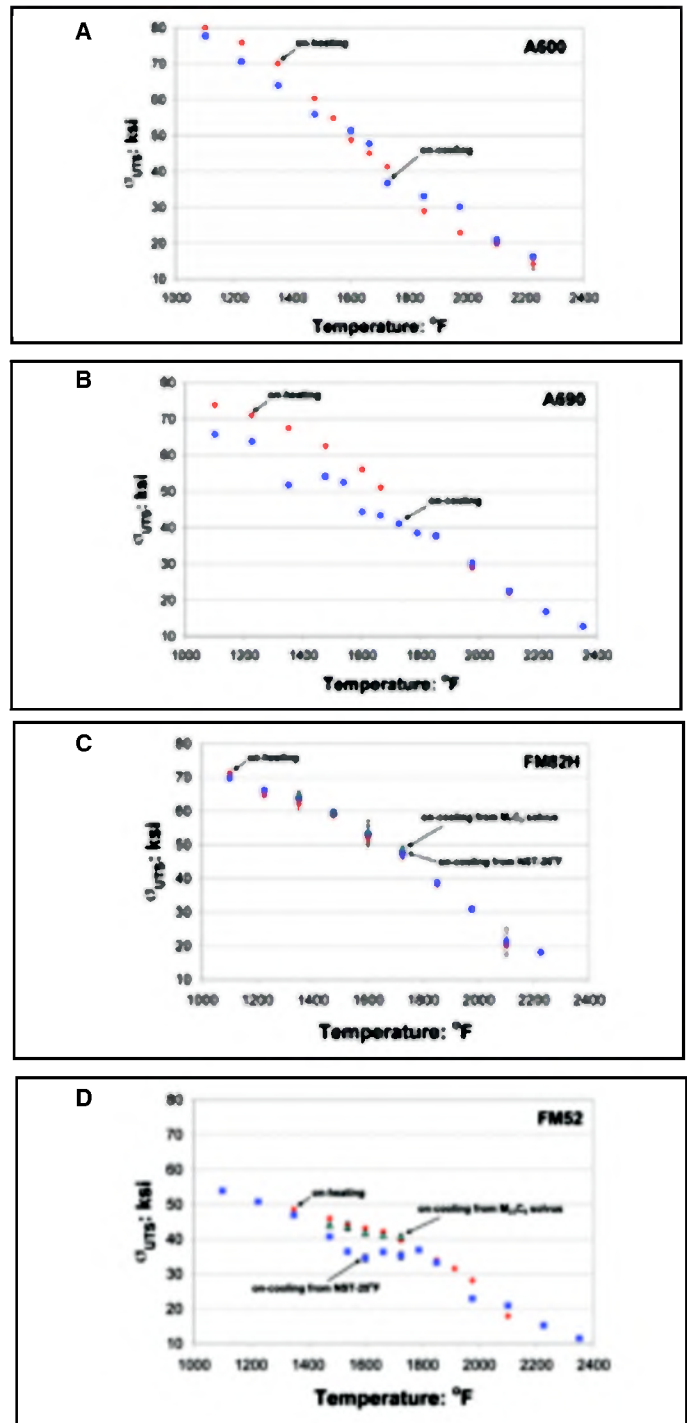


Fig. 6 — On-heating and on-cooling UTS data for the following: A — A600; B — A690; C — FM82H; and D — FM52. FM82H and FM52 UTS curves also include on-cooling data from their respective carbide solvus.

which were machined directly from 1-in.-thick wrought plate.

Testing Parameters and Design

The average cooling rate for this sample design when held in the water-cooled Gleeble® “vacuum jaws,” and allowed to free cool, was approximately 15°F/s (8°C/s). Cooling rates greater than this re-

quired a gas cooling apparatus that was fabricated for this work. It was found that the average cooling rate could be increased to more than 255°F/s (142°C/s) by using a He gas quench. Commercial-grade helium resulted in significant gray oxidation of the samples, therefore Grade 6 helium (99.9999% pure) was used for this work, which resulted in an oxide-free surface finish.

To ensure that liquid films would not form during Gleeble® testing, the Nil Strength Temperature (NST) was determined using procedures outlined elsewhere (Ref. 34). The NSTs for all four alloys are listed in Table 3. Five to six specimens from each alloy condition were tested. From these data, the average NST and 95% confidence interval (CI) were calculated. It was found that a peak temperature correspond-

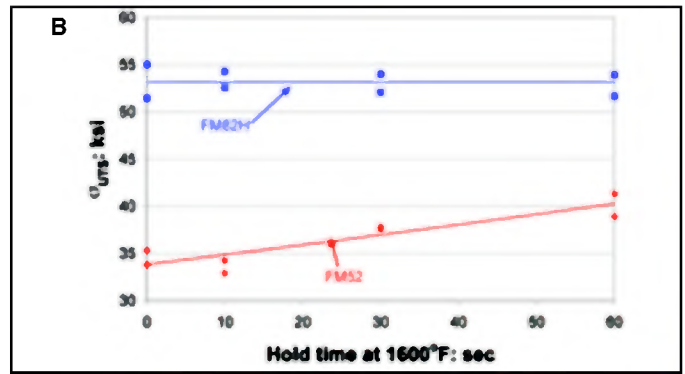
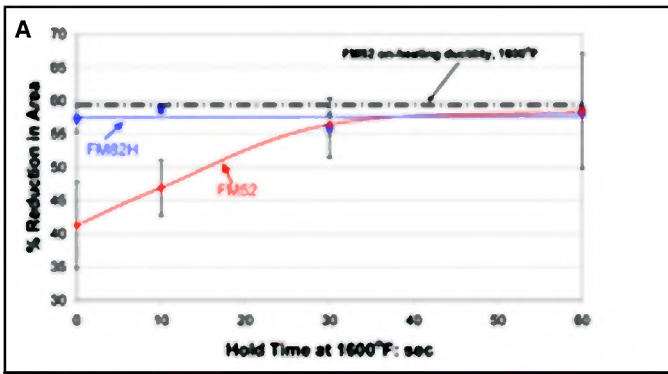


Fig. 7 — Effect of on-cooling hold time at 1600°F. A — Reduction in area; B — UTS.

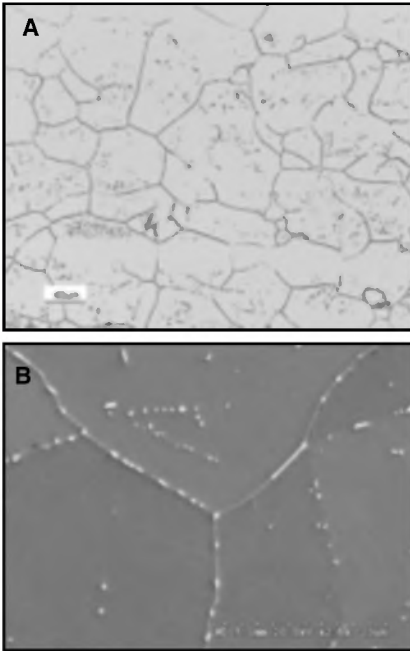


Fig. 8 — As-received A600 micrographs revealing equiaxed grains and grain boundaries decorated with coarse carbides. A — LOM; B — SEM.

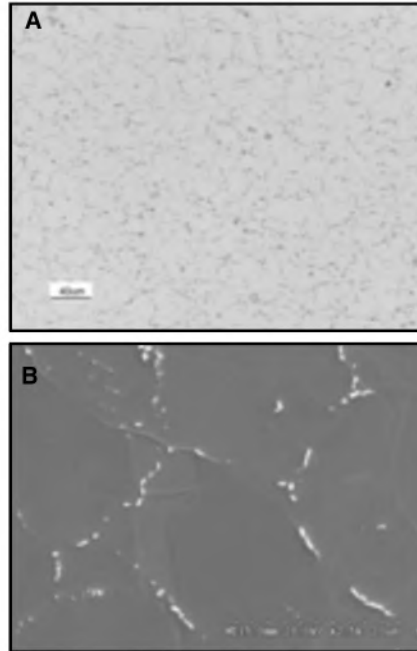


Fig. 9 — As-received A690 micrographs revealing equiaxed grains and grain boundaries decorated with coarse carbides. A — LOM; B — SEM.

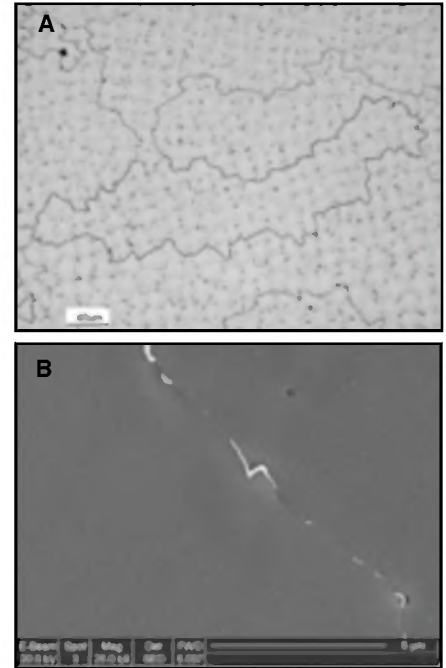


Fig. 10 — As-solidified FM82H micrographs revealing elongated grains and grain boundaries decorated with fine carbides. A — LOM; B — SEM.

ing to the average NST [25°F (13°C)] would provide a 95% confidence that the NST would not be exceeded.

Figure 3 is a graphical depiction of the four thermal cycle conditions tested as part of this work. The locations marked with an X represent temperatures at which hot ductility tests were performed. The heating rate for the on-heating tests was 200°F/s (111°C/s), as shown in Fig. 3A. The cooling rate for all on-cooling tests (Fig. 3B and C) was 90°F/s (50°C/s). He gas quench was used to augment the cooling rate in the “on-cooling” samples because the maximum “free cool” cooling rate that could be obtained was so low (15°F/s). The heating and cooling rates were based upon thermocouple measurements taken from a standard weld joint during typical multipass welding conditions. Samples were hot ductility tested at 125°F (51°C) intervals between 1100°F (593°C) and the peak temperature for

each alloy. Smaller temperature intervals of 62.5°F (17°C) were used in some cases

to provide more detail within temperature ranges of interest.

Table 3 — Nil Strength and Peak Test Temperatures

Alloy	NST ± 95% CI: °F	Peak T, NST-25°F
A600	2446 ± 10	2421
FM82H	2364 ± 17	2339
A690	2447 ± 10	2422
FM52	2428 ± 12	2403

Table 4 — JMatPro Calculated Carbide Solvus Temperatures for the Predominant Carbides in Each Alloy and Maximum Time above Calculated Carbide Solvus Temperatures during Simulated Weld Reheat Thermal Cycle

Alloy	Intergranular Carbide	Calculated Carbide Solvus (°F)	Maximum time above calculated carbide solvus (s)
A600	M ₇ C ₃	1859	9.1
FM82H	MC	2196	2.3
FM82H	M ₇ C ₃	1967	6.0
A690	M ₂₃ C ₆	1972	7.3
FM52	M ₂₃ C ₆	2077	5.3

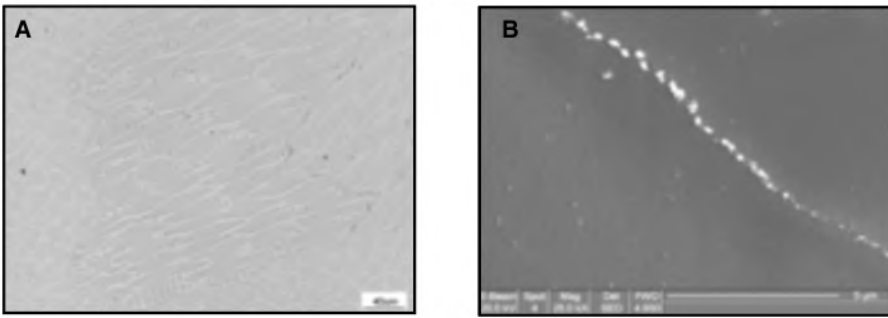


Fig. 11 — As-solidified FM52 micrographs revealing elongated grains and grain boundaries decorated with fine carbides. A — LOM; B — SEM.

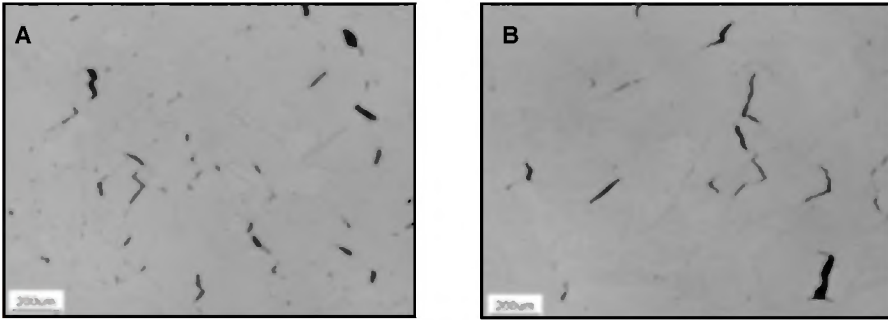


Fig. 12 — LOM micrographs of DDC cracks in A690 hot ductility specimens tested at 1600°F on-cooling. A — Wrought; B — welded condition. Tensile axis is oriented horizontal to the image. These cracks are characteristic of wedge shaped cracks.

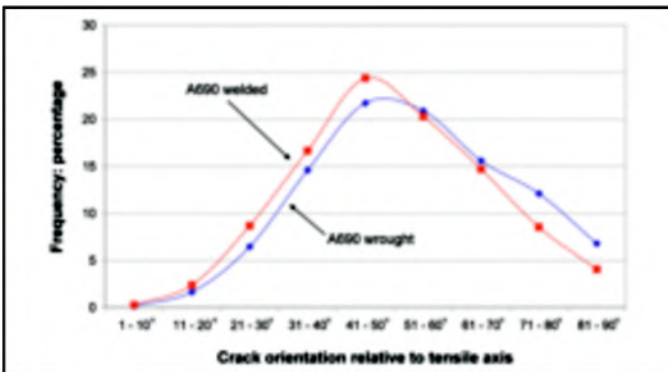


Fig. 13 — Angular distribution of DDC crack orientation with respect to the tensile axis for A690 at 1600°F on-cooling in wrought and welded conditions.

Since several researchers have suggested carbides as contributors to DDC, the effect of carbide dissolution and coarsening/precipitation was investigated through the use of two peak temperatures. The first peak temperature, NST-25°F, was above the carbide solvus of each alloy (see Table 4). It was expected that this would result in some degree of carbide dissolu-

tion — Fig. 3B. The $M_{23}C_6$ and M_7C_3 carbide solvus temperature for FM52 and FM82H, respectively, were used as the other peak temperature — Fig. 3C. No carbide dissolution was expected to occur since the samples were heated to the solvus temperature and then immediately cooled. This thermal cycle would potentially result in carbide coarsening.

Determination of the expected stable carbide and its solvus temperature was necessary for this work. Several carbides can form in FM82H and FM52 based upon their thermal history. Both alloys contain TiC and TiN, which have melting points in excess of 5000°F (2760°C) (Ref.

35), and are thought to be directly transferred from the welding wire (Ref. 12). The predominant second phase in as-solidified FM82H is Nb-rich MC carbide, which forms as a terminal solidification product (Refs. 11, 12). Due to the lack of TTT diagrams for these alloys in the literature, they were calculated using JMatPro, which predicted that M_7C_3 is the second carbide to form after the solid-state MC precipitation reaction in FM82H. The volume fraction of M_7C_3 that forms in FM82H will be a function of the free carbon available after the precipitation of MC carbides. FM52 does not contain significant (<0.01 wt-%) Nb. The predominant carbide formed by the solid-state reaction is $M_{23}C_6$. The JMatPro calculated carbide solvus temperatures for each alloy composition are listed in Table 4. The $M_{23}C_6$ and M_7C_3 carbides were expected to experience the greatest degree of dissolution during the NST-25°F peak temperature. The JMatPro calculated carbide solvus temperatures were found to be in reasonable agreement with values determined experimentally: The $M_{23}C_6$ solvus ranged in temperature from 1868°F (1020°C) and 2024°F (1107°C) in A690 (Refs. 36–39), while the M_7C_3 was found to vary between 1688°F (920°C) and 2012°F (1100°C) in A600 (Ref. 40).

The last thermal cycle evaluated is shown schematically in Fig. 3D. The weld metal alloys were subjected to an isothermal hold for 10 to 60 s at the on-cooling ductility minimum temperature, which was found to be 1600°F (871°C). Based upon the JMatPro calculated TTT diagrams for these alloys, it was expected that this hold would result in carbide precipitation.

DDC susceptibility has been found to increase with decreasing stroke rate in both Invar (Ref. 24) and 310 stainless steel (Ref. 8) when tested on-heating. To date, the effect of stroke rate on DDC susceptibility has not been examined in the alloys under investigation in this work. Therefore, initial work was performed to determine the effect of two different stroke rates (0.004 and 2 in./s: 0.1 and 50.8 mm/s) on A690, which is known to be susceptible to DDC. These stroke rates comprise the upper and lower bounds for Gleeble®-like hot tensile tests (Refs. 24, 41). The effect of stroke rate was evaluated at 1600°F on-heating and on-cooling from the elevated peak temperature. This temperature was chosen because this was shown to be the ductility minimum temperature for multipass weld FM52 specimens (Ref. 42), which have a nominal composition very similar to A690.

All hot ductility testing was performed using a Gleeble® 1500D. For the percent reduction in area (%RA) measurements, the initial cross-sectional area of the samples was measured with micrometers, and

Table 5 — Vickers Micro-Indentation Hardness Values for Various FM52 Thermal Conditions. Note: All Samples Were Unstrained and Water Quenched from Their Respective Temperatures

FM52 condition	HV ± 95% confidence interval
1600°F on-heating	171 ± 3
1600°F on-cooling from NST-25°F	155 ± 2
1600°F on-cooling 60 s hold	165 ± 3
2350°F 10 min hold	146 ± 2

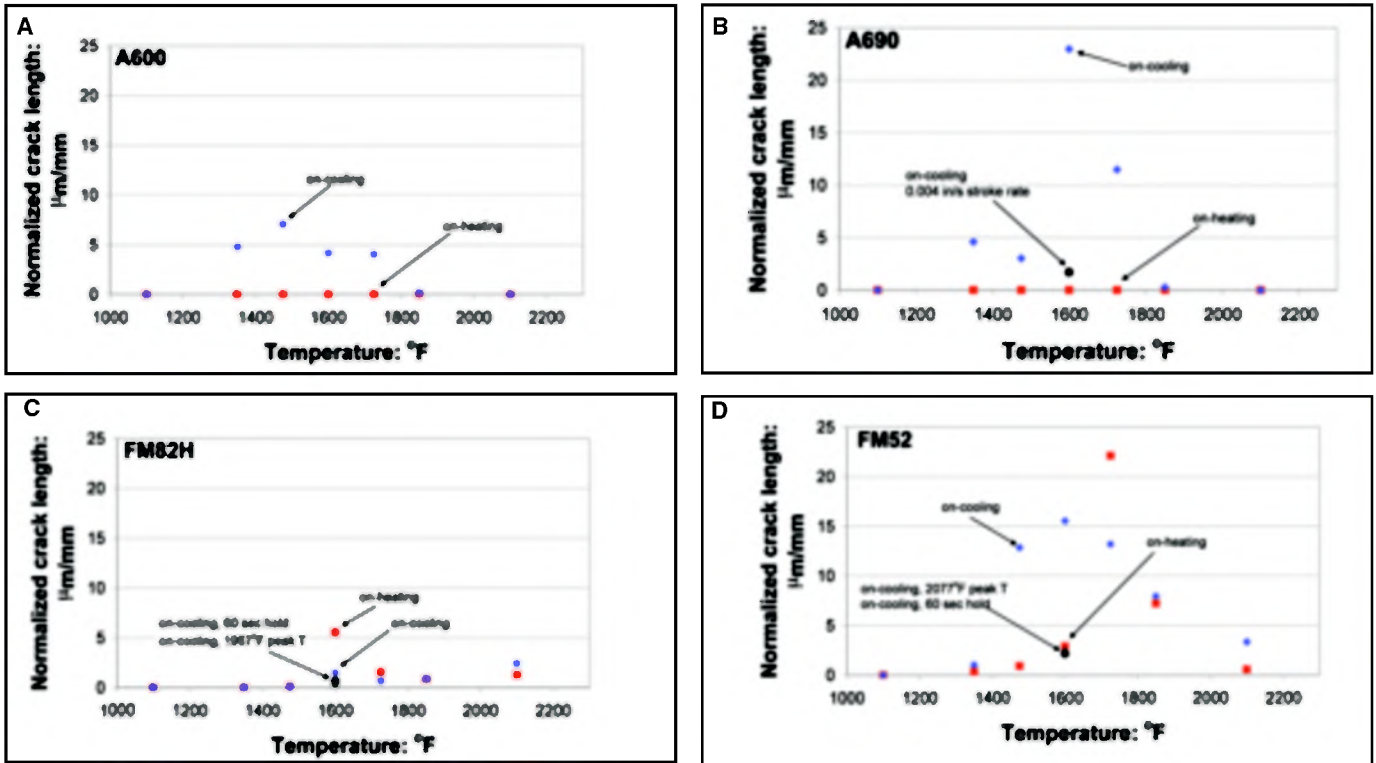


Fig. 14 — Total intergranular crack length per grain boundary length. A — A600; B — A690; C — FM82H; and D — FM52.

the final cross-sectional area was measured using a stereoscope connected to quantitative image analysis software, in a similar fashion as used in other research (Ref. 18). This provided for a more accurate measurement of %RA, particularly in samples where the final cross-sectional shape was not rectangular. Two measurements were made of each fractured surface, resulting in four measurements per tested specimen. The %RA measurement error was found to fall within the size of the data symbols in the hot ductility plots. When multiple samples were tested under the same conditions, the average was plotted with standard deviation error bars. The ultimate tensile strength (UTS) was calculated for each alloy based upon load measurements recorded from Gleeble® load cell data. An acquisition rate of 2000 hertz was used during the loading portion of the test to ensure the peak load could be identified.

Microstructural and Micromechanical Characterization

Select samples were sectioned and mounted in thermosetting epoxy so that the longitudinal-transverse orientation of each test specimen could be viewed. Standard metallographic techniques were used to prepare the samples to a 0.05-µm colloidal silica finish. The samples were then electrolytically etched at 2–3 V for 3–10 s in a solution containing equal parts by volume of water, and sulfuric and phosphoric acid. Bright field light optical microscope (LOM)

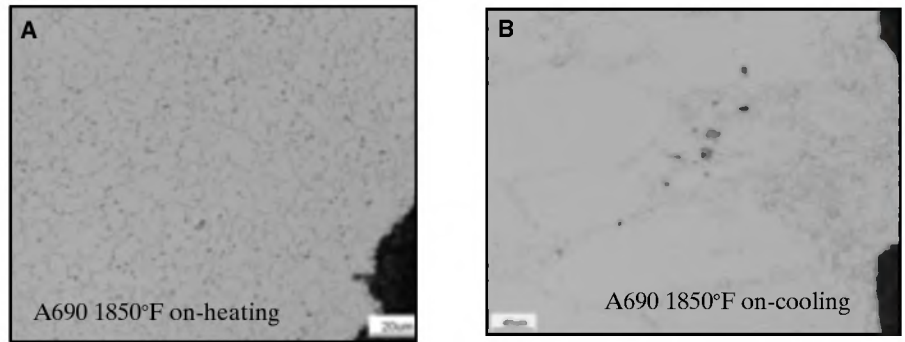


Fig. 15 — LOM images of A690 hot ductility samples revealing dynamically recrystallized grains. A — 1850°F on-heating; and B — 1850°F on-cooling.

images were captured using a Reichert-Jung MF3 metallograph. The angular relationship between grain boundaries that ductility dip cracked and the tensile axis were made using LOM images.

Ductility dip crack length measurements were made using a Nikon Optiphot LOM with a drawing tube attachment that allowed for concurrent viewing of the sample and the cursor of a digitizing pad. Crack length data were normalized with respect to total grain boundary length within a field of measurement so that the cracking behavior of different alloys at various temperatures can be compared on an equal basis. The total grain boundary length within a field of measurement is a function of 1) the surface area of the sample from which crack length was measured and 2) the grain size of the sample. This

normalization was conducted in the following manner. The total grain boundary length within a unit surface area is given by L_{GB}^{Total}/GB (Ref. 43):

$$L_{GB}^{Total} = \left(\frac{\pi}{2} \bar{N}_L \right) \cdot SA \quad (1)$$

where \bar{N}_L is the number of intersections per unit length of line with units of mm^{-1} , and SA is the surface area in mm^2 . This value of N_L can be calculated directly from grain size using the following equation that is derived from ASTM E112 (Ref. 44):

$$\bar{N}_L = 1119.3d^{-0.9993} \quad (2)$$

where grain size (d) is measured in µm. Grain size data were measured for these alloys at select temperatures in the weld

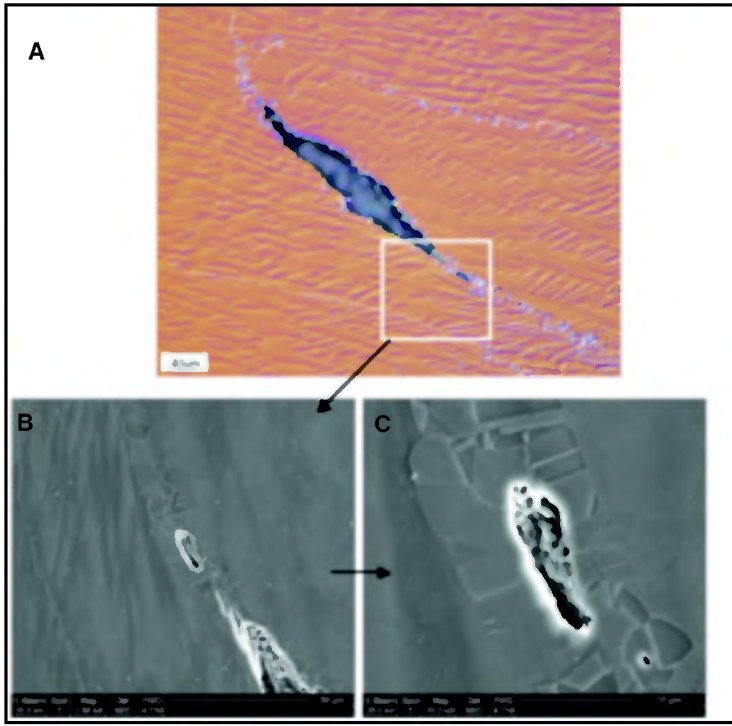


Fig. 16 — Ductility dip crack in FM52 at 2100°F on-cooling as seen using the following: A — Differential image contrast in LOM; B — SEM at low magnification; and C — SEM at high magnification. Recrystallization along grain boundary impedes ductility dip crack growth.

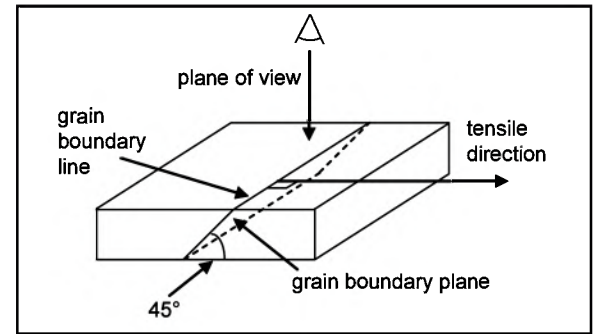


Fig. 17 — Schematic showing how orientation of grain boundary plane with the tensile direction (45 deg) can be different than the grain boundary line with the tensile direction (90 deg).

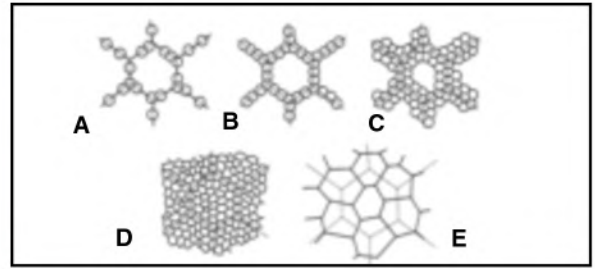


Fig. 18 — Influence of starting grain size on dynamic recrystallization behavior from Ref. 64. A–D show the development of completely recrystallized grain structure when the grain size is large compared to the recrystallized grain size. In E, the initial and recrystallized grains have similar sizes.

thermal cycle using water-quenched specimens. Equation 1 can be combined with Equation 2 to result in the following:

$$L_{GB}^{Total} = \frac{\pi}{2} (1119.3d^{-0.993}) \cdot SA \quad (3)$$

The total measured DDC crack length within any given sample was divided by the total grain boundary length within the field of measurement (L_{GB}^{Total}) to provide the average crack length per length of grain boundary ($\mu\text{m}/\text{mm}$).

The general microstructure and chemistry of second phases were characterized using either an FEI DB 235 or Hitachi 4300 Schottky field emission gun scanning electron microscope (FEG-SEM) with an energy-dispersive spectrometer (EDS). All operation was performed using 20 keV accelerating voltage. An Everhart-Thornley detector, commonly known as a secondary electron detector (SED), was used for all SEM images. The scale markers differ for the two microscopes. Images captured using the Hitachi 4300 use a 10 dot marker with the scale indicated on the lower-right corner of the image. Samples mounted in epoxy were lightly coated with carbon to prevent charging. The above conditions enabled particles as small as 20 nm in size to be resolved.

Lastly, to determine whether the thermal history had an annealing effect on FM52, 20 Vickers micro-indentation

hardness measurements were made on each of four select samples according to ASTM E384 (Ref. 45). All of the specimens were water quenched and unstrained (Ref. 1). The four thermal histories evaluated were 1) 1600°F on-heating, 2) 1600°F on-cooling from the NST-25°F temperature, and 3) 60-s hold at 1600°F on-cooling from the NST-25°F temperature, and 4) 10-min hold at 2350°F (1288°C). The heating and cooling rate (for on-cooling samples) was the same as used above: 200°F/s (111°C/s) on-heating and 90°F/s (50°C/s) on-cooling.

Results

Effect of Stroke Rate

Representative microstructures for the slow stroke rate and fast stroke rate tests performed at 1600°F on-heating and on-cooling are shown in Fig. 4. There was little difference between on-heating and on-cooling ductility for the slow stroke rate samples, which was 82% and 74%RA, respectively. Conversely, the fast stroke rate on-cooling test resulted in a significant ductility loss as compared to the on-heating test using the same stroke rate: 46% vs. 79%RA, respectively. Although 46% is an appreciable degree of ductility, what is significant is that the ductility decreased 42% as compared to the on-heating test.

Microstructurally, this intermediate

temperature on-cooling reduction in ductility was caused by a large number of ductility dip cracks — Fig. 4D, which were not present in the on-heating sample tested at the same stroke rate — Fig. 4C. Both on-heating samples exhibited intergranular cavitation with transgranular void coalescence occurring in the slower stroke rate sample — Fig. 4A. The slower stroke rate, on-cooling sample did have some ductility dip cracks, but they were surrounded by recrystallized grains. The ductility dip cracking was much more severe in the fast stroke rate on-cooling sample. The total normalized DDC crack count in the fast stroke rate on-cooling sample was 23.0 $\mu\text{m}/\text{mm}$ while that for the slow stroke rate on-cooling sample was only 1.7 $\mu\text{m}/\text{mm}$.

These results are significant for several reasons. This is the first investigation into the effect of stroke rate on hot ductility in a Ni-based, solid-solution-strengthened Ni-Cr-Fe alloy. Second, previous researchers showed that slower stroke rates increased DDC in 310 stainless steel (0.1 vs. 100 mm/s) (Ref. 8) and Invar (0.094 vs. 13 mm/s) (Ref. 24); however, this work reveals just the opposite effect for the alloys investigated in this work where faster stroke rates result in more DDC. The causes for these differences in stroke rate and hot ductility behavior are discussed later. Lastly, the faster stroke rate resulted in a more adverse testing condition for DDC, while reproducing the DDC mech-

anism, therefore it was used for all subsequent hot ductility testing.

Mechanical Behavior

The on-heating and on-cooling hot ductility curves for all four alloys are shown in Fig. 5. The on-heating curves of A600 and A690 are similar. The ductility of both alloys degrades on cooling with that of A690 falling below that of A600 between the temperature of 1663°F (906°C) and 1475°F (802°C). The on-cooling ductility from the reduced stroke rate (0.004 in./s) A690 test at 1600°F is also displayed in Fig. 5. This further illustrates the remarkable increase in ductility brought about by using the slower stroke rate. Testing A690 in the as-solidified condition at the ductility minimum temperature (1600°F on-cooling) had no effect on the hot ductility ($37 \pm 3.3\%$ RA) as compared to the wrought condition ($37 \pm 1.9\%$ RA).

In an effort to prevent the formation of carbides, A690 was cooled at approximately 280°F/s (155°C/s) to a temperature within the ductility dip range. The results of two tests are also shown in Fig. 5B. Tripling the cooling rate (90° to 280°F/s) had no effect on the intermediate temperature hot ductility of A690.

The hot ductility of FM82H remains unchanged throughout the weld thermal cycle both on-heating and on-cooling. The on-heating hot ductility of FM52 is higher than that of FM82H at any given temperature on-heating, although there is a small dip in ductility between 1475° and 1775°F (802° and 968°C). When FM52 is cooled from the NST-25°F peak temperature to the intermediate temperature (1663°–1538°F: 906°–837°C), the ductility drops significantly below that of FM82H. The on-cooling hot ductility curves of FM52 and A690 are remarkably similar even though they were tested in two different conditions: wrought and as-solidified for A690 and FM52, respectively.

Peak temperature plays a significant role in the on-cooling behavior of FM52. When cooled from the $M_{23}C_6$ carbide solvus (2077°F), where negligible carbide dissolution is expected to occur, the on-cooling hot ductility is indistinguishable from the on-heating hot ductility. This on-cooling behavior is remarkably different than when FM52 is cooled from the NST-25°F (2403°F). In FM82H, cooling from the M_7C_3 solvus temperature (1967°F) peak temperature resulted in a similar hot ductility as the NST-25°F on-cooling tests.

The on-heating and on-cooling UTS curves for all four alloys are shown in Fig. 6. The on-heating and on-cooling behavior of A600 is relatively unchanged. The on-cooling UTS of A690 is less than it is on-heating at temperatures of 1663°F and below. There is little change in the on-

heating and on-cooling UTS of FM82H. To the contrary, there is a significant intermediate temperature dip in the on-cooling UTS of FM52 as compared to its on-heating behavior. The UTS of FM82H is at least 10% greater than that of FM52 at all points in the thermal cycle and up to 50% greater at intermediate temperatures on-cooling where there is a dip in the UTS of FM52. Much like the %RA results, both FM52 and A690, which are known to be susceptible to DDC, exhibit an on-cooling reduction in UTS.

Modifying the on-cooling thermal cycle significantly affects the UTS of FM52, while that of FM82H remains unchanged. Peak temperature plays an important role in the UTS of FM52. Cooling from the $M_{23}C_6$ carbide solvus eliminates the dip in UTS that is observed when the alloy is cooled from the NST-25°F peak temperature. In FM82H, lowering the peak temperature to the M_7C_3 solvus temperature has little effect on the on-cooling UTS. The effect of isothermal hold time at 1600°F on-cooling from the NST-25°F peak temperature on ductility and UTS are presented in Fig. 7. Ductility and UTS recover in FM52 with hold time at 1600°F, while there is little change in the mechanical behavior of FM82H since the alloy exhibited no initial loss in strength or ductility.

Table 5 shows the results of the micro-indentation hardness measurements that were made on samples that were unstrained and water quenched. As expected, the softest condition was the isothermal hold at 2350°F. The lowest hardness of the three 1600°F conditions was on-cooling from NST-25°F, which is the thermal condition that results in the ductility minimum in FM52.

Microstructural Characterization

Photomicrographs of as-received A600 and A690 are shown in Figs. 8 and 9. The grain boundaries of both alloys are decorated with coarse carbides, although these carbides are different in each alloy. The predominant intergranular carbide in A600 is M_7C_3 (Ref. 46), whereas A690 primarily forms $M_{23}C_6$ (Ref. 47). Additionally, the grain size of A690 is smaller than that of A600. Figures 10 and 11 reveal the as-solidified microstructures for FM82H and FM52, respectively. The carbides are not as prominent in the weld metal alloys

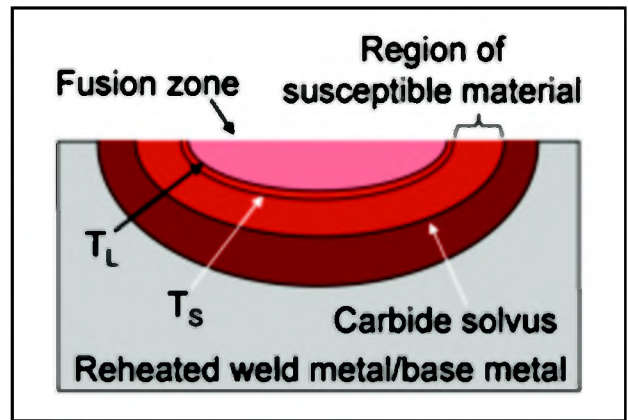


Fig. 19 — Schematic of HAZ where solidus and liquidus temperatures are indicated by T_S and T_L , respectively. Region of HAZ heated above the carbide solvus temperature is made more susceptible to DDC.

as they are in the wrought alloys as evidenced by the SEM micrographs where the magnification for the weld metal alloys is ten times that for the wrought alloys. Both weld metal alloys have larger grain sizes than the wrought materials, which is to be expected. The serrated grain boundary morphology of FM82H is significantly different than the grain boundaries of the other three alloys, which are comparatively straight. A more detailed discussion of each alloy's microstructure is presented elsewhere (Ref. 1).

Figure 12A and B are LOM micrographs taken from A690 hot ductility samples tested at the ductility minimum temperature, 1600°F on-cooling, in the wrought and as-solidified condition, respectively. The tensile axis is oriented horizontal to the image. The appearance of these cracks is characteristic of wedge-type cracks (Ref. 48) that are seen in creep rupture. Qualitatively, these cracks appear to occur on boundaries that are preferentially oriented at a 45-deg angle to the tensile axis. To better quantify this observation, the angle with respect to the tensile axis was measured for more than 600 cracks in each specimen and is shown in Fig. 13. These results confirm that the DDC cracks form preferentially at an angle of approximately 45 deg to the tensile axis. This is the direction at which the shear stress is the highest.

The results of normalized DDC crack length measurements are given in Fig. 14. What is most striking is the absence of DDC in both A600 and A690 when tested on-heating. This is in stark contrast to the on-cooling behavior of both alloys where ductility dip cracks are observed between the temperatures of 1850°F (1010°C) and 1350°F (732°C) for both A600 and A690. The change in on-cooling behavior is particularly remarkable for A690, which had the greatest total crack length all four alloys at 1600°F on-cooling, while no cracks formed at the same temperature on-heating.

ing. The normalized crack length of A690 at this temperature on-cooling was greatly reduced from 23 to 1.7 $\mu\text{m}/\text{mm}$ in the sample tested at the slower stroke rate (0.004 in./s).

Ductility dip cracks were observed in FM82H and FM52 both on-heating and on-cooling. The magnitude of DDC crack length, and the temperature range at which they were observed, was greater for FM52 than FM82H. In general, the amount of DDC in FM52 was greater on-cooling than on-heating, whereas there was little difference between the on-heating and on-cooling cracking behavior of FM82H except at 1600°F on-heating. Cooling from the respective carbide solvus temperature reduces the ductility dip cracking susceptibility of both FM82H and FM52.

Hot ductility samples were examined using LOM to determine the nature and extent of recrystallization. Two general types of recrystallized grain structures were observed in the hot ductility samples: uniform and localized. Figure 15A is a LOM micrograph showing the uniform recrystallization behavior in A690 at 1850°F on-heating. This type of recrystallization behavior was only observed in A600 and A690 samples on-heating, and associated with the greatest resistance to DDC. The second type of recrystallization behavior is shown in Fig. 15B, which is taken from A690 at 1850°F on-cooling. The recrystallized grains are much more localized along the grain boundary. This type of recrystallized grain structure was observed in A600 and A690 on-cooling, and in both FM82H and FM52 on-heating and on-cooling. Localized recrystallized grains were often found ahead of DDC cracks, as shown in Fig. 16 for FM52 at 2100°F on-cooling. This figure also shows that DDC cracks can form at temperatures above the $M_{23}C_6$ carbide solvus (2077°F: 1136°C) where these intergranular carbides have been fully dissolved (Ref. 1) and are not expected to precipitate during hot ductility testing.

Discussion

Much of the recent research into DDC has been performed within the welding community, and it has been viewed as a weldability issue. However, DDC has also been investigated in materials that undergo thermomechanical treatment. As early as the 1960s, intergranular cracks that were formed at temperatures above $0.5 T_m$ were recognized as the most common cause of fracture in hot working of materials (Ref. 49). Hot working is characterized by temperatures above $0.5 T_m$ and strain rates between $10^{-3} - 10^3 \text{ s}^{-1}$ (Ref. 50). This is significant because strain rate and temperature affect deformation mechanisms. Addition-

ally, hot working research has investigated the same range of strain rates and temperatures that have been used in the weldability studies of DDC, including this investigation where the strain rate was between approximately 1 and 2 s^{-1} and the temperature ranged between approximately 0.55 and $0.95 T_m$. Ductility dip cracking has long been observed during the hot working of materials, although not using the DDC nomenclature (Refs. 49–51). Therefore, the hot working literature can be quite useful in furthering the understanding of DDC in weld metal.

Comparison of Ductility and UTS

Using carefully controlled hot torsion quench studies on A600, Shapiro and Dieter found that intergranular cracks formed at the peak torque (Ref. 51). The peak torque is analogous to peak load, or UTS, in the tension (Gleeble®) testing performed in the present investigation. The intermediate temperature dip in ductility in A690 and FM52 also results in a decrease in UTS. Both mechanical measures of DDC have the same root cause: the formation of ductility dip cracks. As these cracks form, they impair an alloy's ability to macroscopically deform and strain harden, thereby decreasing both ductility and the UTS.

Additionally, both ductility and UTS recover with hold time in FM52. Neither exhibits an intermediate temperature dip when FM52 is cooled from the $M_{23}C_6$ solvus temperature (where carbide dissolution is not expected due to the very short time at the solvus temperature). Both mechanical measures of DDC investigated in this work provide reasonable predictions of a material's DDC susceptibility. The advantage of using UTS as a measure of DDC susceptibility is in its simplicity. There are no post-test measurements when using UTS, unlike %RA. Rather, the peak load can be directly obtained from the load cell data generated during the test. It should be noted that UTS may not be a good indicator of DDC susceptibility in other alloy systems and conditions. Further, work may be needed to assess this.

Comparison of Mechanical and Microstructural Data

The crack count data provide insight into how microstructural features (cracks) affect macroscopic properties (ductility and UTS). The ductility minimums in both FM52 and A690 correspond to the peak in maximum crack length per length of grain boundary. The crack count data also reveal key information regarding cracking susceptibility that could not be discerned from the macroscopic measurements of ductility and UTS. The following are sev-

eral examples. First, the on-heating hot ductility data for FM82H are very similar to those of A600 and A690, yet only FM82H forms DDC cracks on-heating. This difference in cracking susceptibility can only be discerned from the microscopic DDC crack measurements (Fig. 5 vs. Fig. 14). Second, the hot ductility of FM52 is similar to, and often higher than, FM82H (Fig. 5) during the on-heating portion of the thermal cycle, yet FM52 has a greater tendency to form DDC — Fig. 14. This difference underscores that mechanical measurements of DDC are not only affected by the formation of DDC cracks, but also by an alloy's ability to dynamically recover and recrystallize. The effects of alloy composition on dynamic recovery and recrystallization must be considered when comparing hot tensile data between alloys. It has been shown that alloying additions of Nb decrease both dynamic recovery and dynamic recrystallization in austenite (Ref. 52). Reducing these two restoration processes may explain why the on-heating ductility between the temperatures of 1100° and 1350°F of FM82H, which contains Nb, is equal to or lower than that of FM52 even though FM82H has higher resistance to DDC than FM52.

Overall, the mechanical and microstructural measures of DDC are complementary. Crack length measurements on fractured hot tensile specimens provide direct information about an alloy's propensity to form ductility dip cracks. However, these measurements do not provide information on the level of stress or strain at which DDC cracks form. The strain at which DDC cracks begin to form can be inferred from the mechanical measures of DDC: ductility and UTS. As DDC cracks nucleate and grow, they form internal free surfaces that decrease the effective cross-sectional area of the sample and impair the alloy's ability to carry a given load. The formation of ductility dip cracks thereby brings about a reduction in UTS as compared to an alloy condition that is more resistant to DDC (e.g., FM52 1600°F on-heating vs. 1600°F on-cooling). Furthermore, the DDC cracks degrade an alloy's ability to deform, which will result in a decrease in %RA since premature fracture will occur due to the nucleation and growth of DDC cracks, as opposed to a purely ductile mechanism, such as microvoid coalescence. The similar on-cooling hot ductility behavior of A690 and FM52 indicate that DDC cracks form at approximately the same level of strain, even though their grain size is significantly different: $93 \pm 13 \mu\text{m}$ vs. $263 \pm 13 \mu\text{m}$, for A690 and FM52, respectively at 1600°F

on-cooling (Ref. 1).

While the specific reason for the particularly high value at 1725°F for FM52 on-heating is currently not known, as pointed out in the discussion section, the high value of normalized crack length generally correlates with the minimum in ductility (i.e., compare Figs. 5 and 14). Reasonable agreement exists between the macroscopic mechanical measures of DDC and microscopic cracking susceptibility; therefore, the hot ductility test reliably predicts which alloys will exhibit a greater tendency to DDC.

Microstructural Factors Affecting Ductility and UTS

Qualitatively, it has been suggested that DDC cracks form over a preferred orientation of angles oriented between 45 and 90 deg to the tensile axis (Ref. 9). This qualitative observation appears consistent with the cracking observations for A690 at the on-cooling ductility minimum (1600°F) as seen in Fig. 12. Quantification of these cracking data shows that there is indeed a preference for cracks to form along boundaries oriented 45 deg to the tensile axis (Fig. 13), for samples tested in wrought and as-solidified condition, which is the angle at which maximal shear is expected to occur. However, the distribution of cracks is not normal about 45 deg, which would be expected if grain boundary sliding was an operative mechanism in DDC. Rather, the distribution is skewed to higher angles. The distribution for the wrought data is more skewed than it is for the as-solidified. This difference in these two distributions is probably due to the difference in grain shape. The wrought sample consisted of equiaxed grains, whereas the grains in the as-solidified sample were preferentially oriented with respect to the tensile axis, thereby introducing some bias into the crack orientation measurement.

Nonetheless, both the wrought and as-solidified data are not normal about 45 deg. This is due to the limitations of the stereological technique employed. Figure 17 is a schematic illustration that shows how a grain boundary plane may be oriented within a given volume of material. In this instance, the intersection of the grain boundary plane with the plane of view forms a grain boundary line that is orientated at a 90-deg angle to the tensile axis. This is the angle that is measured using standard image analysis techniques. In reality, the angle between the grain boundary plane and the tensile axis is at 45 deg. It is not possible to measure this angle from a single plane of view. Ideally, the orientation of the grain boundary plane could be plotted as a function of angle with

respect to the tensile direction. Some attempts have been made to correct for the limitations of measuring the orientation of the grain boundary line to the tensile axis. Scriven and Williams attempted to measure the angular distribution of cavitated boundaries in copper that was subjected to fatigue testing at 400°C (Ref. 53). Their angular distribution curve is very similar to that seen in Fig. 13 for DDC cracking in A690. They concluded that this type of angular distribution demonstrates that boundaries oriented in the direction of maximal shear preferentially cavitated. With reference to DDC of A690, grain boundaries oriented along the direction of maximal shear force are most likely to ductility dip crack. This suggests that grain boundary sliding is an operative mechanism in DDC.

Furthermore, the ductility dip cracks in both the wrought and as-solidified samples (Fig. 12) are shaped like wedge-type cracks (w-cracks) that are observed during creep at high stresses and low temperature (Ref. 54). It is widely accepted that wedge-type cracks are formed as a result of grain boundary sliding (GBS) (Refs. 48, 54–57). There are two general types of GBS: Lifshitz and Rachinger (Ref. 58). Lifshitz sliding is the direct result of stress-directed diffusion of vacancies, whereas Rachinger sliding is accommodated by intragranular deformation (Ref. 58). During Rachinger GBS, the grain boundaries remain contiguous if the intragranular deformation can fully accommodate the GBS. Wedge-type cracks form when intragranular slip occurs at a slower rate than GBS. As such, alloy changes that impede intragranular slip but do not also decrease GBS would be expected to increase the propensity to form wedge cracks. This may be the case with A690 and A600, which are both solid-solution-strengthened alloys. Alloy 690 contains approximately 15 wt-% more chromium than A600, and is also more susceptible to DDC. The increased chromium concentration in A690 may sufficiently strengthen the grain interior to disrupt the balance of GBS and intragranular slip necessary to avoid intergranular cracking. Similarly, the susceptibility to form wedge cracks could be decreased by changes to the alloy that impede grain boundary sliding, like the formation of intergranular precipitates and/or serrated grain boundaries. As discussed in the second paper in this series, both A690 and FM52 have fewer obstacles to grain boundary sliding at the ductility minimum temperature than either A600 or FM82H (Ref. 1). The combined increase in intragranular strength and decrease in resistance to GBS may significantly contribute to the DDC susceptibility of A690 and FM52.

Wedge-type cracks have been observed in the hot torsion of Nickel 270 at tempera-

tures ranging from 800°F (427°C) up to 2000°F (1093°C) with strain rates up to 70 s⁻¹ (Ref. 59). However, wedge cracks are not expected to form during hot tension testing of nickel at strain rates higher than 1 s⁻¹ for temperatures less than 1700°F (927°C) (Ref. 55). This indicates that the difference in loading condition (tension vs. torsion) may affect the formation of wedge cracks. Nonetheless, in this current work DDCs form as wedge-type cracks; therefore, GBS appears to play a significant role in DDC given the test conditions employed.

Dynamic recrystallization has been cited by several authors in the welding literature as an elevated temperature recovery mechanism that brings about an increase in hot ductility at temperatures above the ductility dip temperature (Refs. 11, 26, 60). Recovery and recrystallization are the two general classes of restoration processes that reduce the internal energy of a deformed material. Recovery consists of the rearrangement of dislocations into low angle boundaries, which delineate subgrains. Recovery requires that the dislocations be able to climb and cross-slip, which are hindered in materials with moderate to low stacking fault energy where the dislocations disassociate into partial dislocations. In materials with low stacking fault energy, recrystallization is the preferred method of recovery since the climb and cross-slip of dislocations is not necessary (Ref. 61). Rather, new unstrained grains form at locations of high lattice strain energy that is brought about by inhomogeneities in the deformed microstructure. These can include grain boundaries, twin intersections, and shear bands (Ref. 62).

Dynamic recrystallization (DRX) is a function of strain rate, temperature, stored deformation energy in the form of dislocations, and grain size (Refs. 63, 64). Forming dynamically recrystallized grains significantly increases ductility (Ref. 50). The noticeable increase in on-heating hot-ductility in A600 and A690 at temperatures of 1600°F (871°C) and above can be explained by the increase in dynamically recrystallized grains. One way dynamically recrystallized grains act to increase ductility at elevated temperatures is by preventing ductility dip crack propagation. This can be seen in Fig. 16 where the ductility dip crack is completely surrounded by recrystallized grains that prevent its further growth.

In the micrographs for A690 shown in Fig. 15A and B, the strain rate and temperature (1850°F) are the same; however, there is a significant difference in recrystallization behavior. This can be explained by a change in intergranular carbide distribution that affects both grain size and the delocalization of grain boundary stresses. The intergranular carbides observed in as-received A690 (Fig. 9B) dissolve during the peak temperature portion

of the thermal cycle that is above the $M_{23}C_6$ solvus temperature, which results in grain growth. The average grain size of A690 at 1850°F on-heating is approximately 30 μm , while that at 1850°F on-cooling is 88 μm (Ref. 1). Grain size has a significant effect on DRX. In austenite it has been shown that smaller initial grain sizes decrease 1) the critical strain required for dynamic recrystallization and 2) the temperatures required for DRX given a certain strain (Ref. 65). Furthermore, recrystallized grains will tend to localize along the grain boundary and form a necklace structure as the initial grain size increases (Ref. 63). A similar effect also occurs in A600 where the dissolution of M_7C_3 results in an increase of on-cooling grain sizes and localization of dynamically recrystallized grains to the grain boundaries.

The dissolution of intergranular precipitates acts in three ways to affect the dynamic recrystallization behavior. The first way is by localizing grain boundary stresses. Bruemmer et al. (Refs. 66, 67) performed a series of elegant in-situ deformation studies of A600 using a high-voltage electron microscope (HVEM) to study the effects of intergranular precipitates on deformation behavior of A600. Intergranular precipitates were found to be the principal dislocation sources in A600. These intergranular precipitates acted to delocalize stresses that formed along grain boundaries during deformation. This resulted in more homogenous plastic deformation in A600 samples that were heat treated in order to form a high density of intergranular precipitates (Ref. 67). Conversely, A600 that was subjected to a thermal treatment that resulted in fewer intergranular carbides exhibited deformation that was localized to the region surrounding the grain boundary (Ref. 67). Based on this, it is expected that fewer intergranular carbides will result in strain localization along grain boundaries, and further prevent complete dynamic recrystallization.

The second way dissolution of intergranular carbides affects DRX is by increasing the susceptibility of grain boundaries to DDC cracking. Forming ductility dip cracks generates internal free surfaces that can no longer bear the loading force. This decreases the amount of deformation energy that the material can effectively convert into strain energy. This decrease in strain energy in the crystal reduces the driving force to bring about complete DRX.

Thirdly, dissolution of intergranular carbides increases the grain size. When the grain size is large compared to the recrystallized grain size the DRX grains will first form along grain boundaries, then additional DRX grains will form into the grain

interior as deformation increases. This is seen in Fig. 18A–D (Ref. 63) where a necklace structure of DRX grains forms along the grain boundaries when the initial grain size is significantly larger than the recrystallized grain size. With increasing deformation, the necklace structure is filled up with additional DRX grains. However, if DDC cracks form this process will be interrupted. When the initial and recrystallized grain sizes are similar, recrystallized structure will appear like that shown in Fig. 18E. This later structure is what is observed in both A600 and A690 at temperatures above 1600°F on-heating — Fig. 15A and B.

Due to their role in delocalizing grain boundary stresses, intergranular precipitates may act to inhibit DDC nucleation. Thermal cycles that promote carbide precipitation/coarsening result in decreased DDC normalized crack length, as can be seen in Fig. 14. This is observed when the peak temperature is lowered to the respective carbide solvus temperatures in FM82H and FM52, and when these alloys are subjected to an isothermal hold at 1600°F for 60 s. An increase in intergranular carbide precipitation is also expected to occur in the slow stroke rate testing performed on A690 at 1600°F. The time under load in this condition was approximately 90 s, which is longer than the isothermal hold time required to recover the hot ductility of FM52 (which has nearly the same nominal composition as A690) at the same temperature. The decrease in strain rate is also expected to lower the critical strain required to form dynamically recrystallized grains, as has been shown in Ni and Ni-Fe alloys (Ref. 68). This can be seen qualitatively in Fig. 4B and D where there are significantly more dynamically recrystallized grains in the slow stroke sample tested at 1600°F on-cooling.

Whereas thermal cycles that resulted in the dissolution of intergranular carbides were found to increase DDC susceptibility, modifications to the thermal cycle that promoted the formation of intergranular carbides decreased DDC susceptibility. In particular, an isothermal hold at the on-cooling ductility minimum for FM52, 1600°F, resulted in a recovery of both ductility and UTS. Time at elevated temperature can allow for recovery and recrystallization to soften an alloy, which may lead to an increase in ductility. Therefore, microhardness measurements were made on unstrained samples of FM52 that underwent four different thermal treatments followed by a water quench. The ductility minimum temperature, 1600°F, is the temperature of interest; therefore, microhardness measurements were made on 1600°F samples in three different conditions: 1) on-heating, 2) on-cooling from NST-25°F, and 3) on-cooling from NST-25°F followed by a 60-s hold. The hardness of these three samples was

compared to a fourth sample that acted as a control, which was subjected to a thermal treatment that would be expected to result in softening: an isothermal hold at 2350°F (1288°C) for 10 min. The results reveal that the 1600°F on-cooling from NST-25°F sample had the lowest hardness of the three 1600°F thermal conditions (Table 5). Only the sample subjected to a 10-min hold at 2350°F was softer. The higher hardness of both the 1600°F on-heating and 60-s hold sample is most likely due to their higher volume fraction of $M_{23}C_6$ precipitates. This shows that the recovery of ductility in FM52 with hold time is not the result of annealing.

FM82H consists of two microstructural features that work to its advantage in preventing DDC nucleation and propagation. The most obvious distinctive feature of FM82H are the serrated grain boundaries (Fig. 10A), which are expected to be highly resistant to grain boundary sliding. Less obvious is the stability of the Nb-rich MC carbides that form in FM82H, which is much more stable during the peak temperature portion of the thermal cycle than the $M_{23}C_6$ (A690 and FM52) and M_7C_3 (A600) intergranular carbides (Ref. 1). These carbides likely act to further impede grain boundary sliding and DDC nucleation.

It should be noted that DRX is generally not observed adjacent to DDC cracks in multipass welds. This is probably a result of the lower levels of strain that the alloys experience during multipass welding as compared to hot ductility testing. Increasing total strain promotes DRX. However, as this work shows, the faster strain rate results in a greater loss of on-cooling ductility at the ductility dip temperature. Furthermore, the DDC mechanism is reproduced in the hot ductility test, even if the recovery mechanisms observed in the hot ductility test may not be operative in multipass welds.

Further Insights Into the Mechanism of DDC

The results in this work show that intergranular precipitates play a key role in suppressing ductility dip cracking. As mentioned previously, thermal cycles designed to dissolve precipitates increase an alloy's tendency to localize strain along the grain boundaries and form DDC. Conversely, thermal cycles that result in precipitation and growth of intergranular carbides decrease DDC susceptibility. The following test conditions all promoted intergranular precipitation and all resulted in decreased DDC susceptibility:

1. Cooling FM82H and FM52 from their respective carbide solvus temperatures
2. Isothermal hold at the on-cooling ductility minimum temperature
3. Slower stroke rate at on-cooling ductility minimum temperature.

This work indicates that regions of the reheated weld metal where the peak temperature exceeds the intergranular carbide solvus temperature will be made vulnerable to DDC. This is shown schematically in Fig. 19 where several key isotherms are overlaid onto a HAZ. Regions heated above the carbide solvus, but below the liquidus, are expected to become more vulnerable to DDC. The size of this vulnerable region of weld metal can be decreased by forming intergranular precipitates that are stable at higher temperature, as is the case in NbC forming FM82H.

Ductility dip cracking forms preferentially along grain boundaries oriented at a 45-deg angle with respect to the tensile axis. This indicates that grain boundary sliding plays a role in DDC. Furthermore, DDC cracks are observed at temperatures above the $M_{23}C_6$ carbide solvus for FM52 (2100°F (1149°C)) both on-heating and on-cooling. This can be explained by grain boundary sliding, but not by the current form of the precipitation-induced cracking hypothesis (Refs. 19, 29) since at 2100°F $M_{23}C_6$ carbides in FM52 are 1) not present and 2) not expected to form during the hot ductility test since the test temperature is above the $M_{23}C_6$ solvus (2077°F (1136°C)). Further insights into the DDC mechanism and the influence of microstructural condition on DDC susceptibility will be discussed in the Part II companion paper (Ref. 1).

Conclusions

The DDC susceptibility of Alloys 600 and 690 have been investigated along with their companion filler metals (FM52 and FM82H, respectively) using a combination of Gleeble® hot ductility testing and microstructural characterization techniques. The following conclusions can be drawn from this research:

1. A high stroke rate (2 in./s (50.8 mm/s)) resulted in greater DDC susceptibility in the Gleeble® hot ductility test than a slower stroke rate (0.004 in./s (0.1 mm/s)) at the ductility minimum temperature of 1600°F on-cooling. Slower stroke rates are expected to result in more intergranular precipitation and dynamic recrystallization.

2. Ductility and UTS are reliable macroscopic indicators of DDC in the solid-solution-strengthened, Ni-based alloys tested in this work. Additionally, they provide an indirect measure of when DDC begins to form in an alloy.

3. Crack count measurements on hot ductility specimens provide a more direct assessment of cracking susceptibility than macroscopic mechanical measures (ductility and UTS); however, crack counts are much more time consuming and do not provide information on the strains/stresses required to form DDC.

4. The greatest resistance to DDC was observed in A600 and A690 at all temperatures on-heating. Strain was uniformly distributed within these samples as evidenced by uniform dynamically recrystallized grains.

5. The hot ductility of FM52 and A690, both of which are susceptible to DDC, both dipped well below the minimum ductility of A600 and FM82H when cooled from a near NST peak temperature.

6. In general, alloys were most susceptible to form DDC when cooled from a peak temperature near the NST of the alloy and tested at an intermediate temperature corresponding to a homologous temperature of approximately 0.72.

7. Peak temperature has a significant effect on the on-cooling DDC susceptibility of FM52. DDC resistance is increased when FM52 is cooled from the $M_{23}C_6$ solvus temperature, as compared to the super solvus NST-25°F peak temperature. The near NST peak temperature results in the dissolution of intergranular $M_{23}C_6$ carbides (Ref. 1), which promotes grain boundary sliding and DDC.

8. Hot ductility and UTS can be recovered in FM52 by isothermally holding at the ductility minimum temperature for 60 s. This recovery is not associated with an annealing effect. This recovery appears to be the result of decreased susceptibility to grain boundary sliding due to increased intergranular carbide coverage.

Acknowledgments

This work was funded by a Naval Nuclear Propulsion Program Fellowship sponsored by Naval Reactors Division of the U.S. Department of Energy. The authors would like to thank Dr. George Young Jr., Tom Capobianco, Steve Rooney, and Dan Bozik of Lockheed Martin for their assistance in this work. Additionally, Noecker thanks Dr. Tom Lienert of Los Alamos National Laboratory for his continuing interest in this work and helpful discussions.

References

1. Noecker II, F. F., and DuPont, J. N. 2007. Metallurgical investigation into ductility dip cracking in Ni-based alloys: Part II — Microstructural and microchemical development is characterized during simulated weld reheat thermal cycle and correlated to ductility dip cracking susceptibility. Submitted for publication to the *Welding Journal*.
2. International Energy Agency. 2007. *Key World Energy Statistics — 2007*. http://www.iea.org/Textbase/publications/free_new_Desc.asp?PUBS_ID=1199.
3. Saunders, S. 2007–2008. *Jane's Fighting Ships*. Alexandria, Jane's Information Group, 801.
4. Bamford, W. H. J. 2003. A review of Alloy 600 cracking in operating nuclear plants: Histor-

ical experience and future trends. *Eleventh International Conference on Environmental Degradation of Materials in Nuclear Power Systems—Water Reactors*. W. Stevenson, 1071–1081. American Nuclear Society.

5. Gorman, J. A., and Staehle, R. W. 2001. Corrosion problems in the nuclear power industry and implications for the future. *Proceedings of Chemistry and Electrochemistry of Corrosion and Stress Corrosion Cracking Symposium*. R. H. Jones and R. W. Staehle, 397–419. TMS.

6. Harrod, D. L., Gold, R. E., and Jacko, R. J. 2001. Alloy optimization for PWR steam generator heat-transfer tubing. *JOM* 53(7): 14–17.

7. Strauss, S. D. 1996. Inconel 690 is alloy of choice for steam-generator tubing. *Power* 140(2): 29–30.

8. Nissley, N. E., and Lippold, J. C. 2003. Development of the strain-to-fracture test: A new test has been established for evaluating ductility dip cracking susceptibility in austenitic alloys. *Welding Journal* 82(12): 355-s to 364-s.

9. Collins, M. G., and Lippold, J. C. 2003. An investigation of ductility dip cracking in nickel-based filler materials. Part I: The strain-to-fracture test has been used to develop temperature-strain relationships for ductility dip cracking. *Welding Journal* 82(10): 288-s to 295-s.

10. Collins, M. G., Ramirez, A. J., and Lippold, J. C. 2003. An investigation of ductility dip cracking in nickel-based weld metals. Part II: Fracture behavior and fracture surface morphology are related to microstructure, composition, and temperature. *Welding Journal* 82(12): 348-s to 354-s.

11. Collins, M. G., Ramirez, A. J., and Lippold, J. C. 2004. An investigation of ductility-dip cracking in nickel-based weld metals. Part III: The characteristics of weld-metal grain boundaries associated with elevated-temperature fracture are investigated. *Welding Journal* 83(2): 39-s to 49-s.

12. Ramirez, A. J., and Lippold, J. C. 2004. High temperature behavior of Ni-base weld metal. Part I: Ductility and microstructural characterization. *Materials Science & Engineering A* A380(1-2): 259–271.

13. Ramirez, A. J., and Lippold, J. C. 2004. High temperature behavior of Ni-base weld metal. Part II: Insight into the mechanism for ductility dip cracking. *Materials Science & Engineering A* A380(1-2): 245–258.

14. Ramirez, A. J., Sowards, J. W., and Lippold, J. C. 2006. Improving the ductility-dip cracking resistance of Ni-base alloys. *Journal of Materials Processing Technology* 179(1–3): 212–218.

15. Nishimoto, K., Saida, K., and Okauchi, H. 2006. Microcracking in multipass weld metal of Alloy 690. Part 1: Microcracking susceptibility in reheated weld metal. *Science and Technology of Welding and Joining* 11(4): 455–461.

16. Nishimoto, K., Saida, K., Okauchi, H., and Ohta, K. 2006. Microcracking in multipass weld metal of Alloy 690. Part 2: Microcracking mechanism in reheated weld metal. *Science and Technology of Welding and Joining* 11(4): 462–470.

17. Nishimoto, K., Saida, K., Okauchi, H., and Ohta, K. 2006. Microcracking in multipass weld metal of Alloy 690. Part 3: Prevention of microcracking in reheated weld metal by addition of La to filler metal. *Science and Technology of Welding and Joining* 11(4): 471–479.

18. Dave, V. R., Cola, M. J., Kumar, M., Schwartz, A. J., and Hussen, G. N. A. 2004.

Grain boundary character in Alloy 690 and ductility-dip cracking susceptibility. *Welding Journal* 83(1): 1-s to 5-s.

19. Young, G. A., Capobianco, T. E., and Etien, R. 2007. Development of a highly weldable and corrosion resistant Ni-Cr filler metal. Degradation 2007: 13th International Conference on Environmental Degradation in Nuclear Power Systems. Eds. T. R. Allen, J. T. Busby, and P. T. King, compact disc (CD). Canadian Nuclear Society.

20. Nishimoto, K., Mori, H., and Hirata, H. 2001. Effect of grain boundary segregation of sulphur on reheat cracking susceptibility in multipass weld metal of Fe-36%Ni alloy. *Today and Tomorrow in Science and Technology of Welding and Joining, Proceedings of the 7th Japanese Welding Society International Symposium*. T. Ohji, pp. 827-832. Japan Welding Society.

21. Nishimoto, K., Hongou, S., Kubo, N., Koga, S., Nagatani, H., Ogawa, K., and Hirata, H. 2001. Hot cracking and its prevention in multipass weld metal of Fe-36% Ni Invar alloy. *Today and Tomorrow in Science and Technology of Welding and Joining, Proceedings of the 7th Japanese Welding Society International Symposium*. T. Ohji, pp. 833-838. Japan Welding Society.

22. Nakagawa, H., Matsuda, F., Nagai, A., and Sakabata, N. 1980. Weldability of Fe-36%Ni alloy report I: Hot cracking with cross-bead test. *Trans. JWRI* 9(2): 55-62.

23. Matsuda, F., Nakagawa, H., Minehisa, S., Sakabata, N., Ejima, A., and Nohara, K. 1984. Weldability of Fe-36% Ni alloy report II: Effect of chemical composition on reheated hot cracking in weld metal. *Trans. JWRI* 13(2): 69-75.

24. Zhang, Y. C., Nakagawa, H., and Matsuda, F. 1985. Weldability of Fe-36%Ni alloy report III: Dynamic observation of reheat hot crack and evaluation of hot ductility of reheated weld metal. *Trans. JWRI* 14(1): 107-114.

25. Zhang, Y. C., Nakagawa, H., and Matsuda, F. 1985. Weldability of Fe-36%Ni alloy report IV: Dynamic observation of reheat hot cracking in weld metal by means of hot stage microscope. *Trans. JWRI* 14(2): 113-117.

26. Zhang, Y. C., Nakagawa, H., and Matsuda, F. 1985. Weldability of Fe-36%Ni alloy report V: Behaviors of grain-boundary sliding and cavity formation preceding reheat hot cracking in weld metal. *Trans. JWRI* 14(2): 119-124.

27. Zhang, Y. C., Nakagawa, H., and Matsuda, F. 1985. Weldability of Fe-36%Ni alloy report VI: Further investigation on mechanism of reheat hot cracking in weld metal. *Trans. JWRI* 14(2): 125-134.

28. Rhines, F. N., and Wray, P. J. 1961. Investigation of the intermediate-temperature ductility minimum in metals. *Am. Soc. Metals, Trans. Quartz* 54(2): 117-128.

29. Young, G. A., Capobianco, T. E., Penik, M. A., Morris, B. W., and McGee, J. J. 2007. The mechanism of ductility dip cracking in nickel-chromium alloys. *Welding Journal* 87(2): 31-s to 43-s.

30. Adonyi, Y., and Blodgett, O. 2006. Heat-affected zone characterization by physical simulations. *Welding Journal* 85(10): 42-47.

31. Savchenko, V. S., Yushchenko, K. A., and Savolei, N. I. 1988. Effect of strain rate on the hot cracking susceptibility of stable austenitic welded joints in the low temperature brittleness range. *Welding International* 2(10): 874-877.

32. Saunders, N., Guo, Z., Li, X., Miodownik, A. P., and Schille, J. P. 2003. Using JMatPro to model materials properties and behavior. *JOM* 55(12): 60-65.

33. Saunders, N., Guo, Z., Li, X., Miodownik, A. P., and Schille, J. P. 2004. Modeling the material properties and behaviour of Ni-based superalloys. *Proceedings of the 10th International Symposium on Superalloys*. Eds. K. A. Green et al., pp. 849-858. TMS.

34. Low force jaw set for Gleeble® systems: Model 9510 series jaw sets information manual. Dynamic Systems Inc.

35. Schwartz, M. M. 1990. *Ceramic Joining*. Materials Park, Ohio: ASM International, 4.

36. Isoard, V., and Rack, H. J. 1997. High temperature grain growth in Inconel 690. *THERMEC '97, International Conference on Thermo-mechanical Processing of Steels and Other Materials*, 2nd. Eds. T. Chandra and T. Sakai, pp. 1737-1744. TMS.

37. Diano, P., Muggeo, A., Van Duysen, J. C., and Guttman, M. 1989. Relationship between microstructure and mechanical properties of Alloy 690 tubes for steam generators. *Journal of Nuclear Materials* 168(3): 290-294.

38. Lee, J. A., Lee, J. H., Kim, J. J., and Chai, Y. S. 2005. Effects of heat treatment condition on the microstructure evolution of Inconel 690. *Key Engineering Materials* 297-300(1): 458-462.

39. Lim, Y. S., Hwang, S. S., Suh, J. H., and Kim, J. S. 2001. Grain growth and intergranular carbide precipitation in nickel-base Alloy 690. *Recrystallization and Grain Growth, Proceedings of the 1st Joint International Conference*. Eds. G. Gottstein and D. A. Molodov, pp. 389-394. Springer-Verlag.

40. Scarberry, R. C., Pearman, S. C., and Crum, J. R. 1976. Precipitation reactions in Inconel Alloy 600 and their effect on corrosion behavior. *Corrosion* 32(10): 401-406.

41. Lundin, C. D., Qiao, C. Y. P., and Lee, C. H. 1990. Standardization of Gleeble® hot ductility testing. Part II: Experimental evaluation. *Proceedings of Materials Weldability Symposium*. Eds. R. A. Patterson and K. W. Mahin, pp. 9-22. ASM International.

42. Noecker II, F. F., DuPont, J. N., Capobianco, T. E., Young Jr., G. A., Jordan, C. E., Lewis, N., and Burke, M. G. 2005. Microstructural characterization and hot ductility of nickel based weldments. American Welding Society Conference, Dallas, Tex.

43. Russ, J. C., and Dehoff, R. T. 2000. *Practical Stereology, 2nd Edition*. New York: Kluwer Academic/Plenum Publisher, 56.

44. *Standard Test Methods for Determining Average Grain Size*. 1996. ASTM E112-96. Conshohocken, Pa.: American Society for Testing and Materials.

45. *Standard Test for Microhardness of Materials*. 2005. ASTM E384 A. Conshohocken, Pa.: American Society for Testing and Materials.

46. Inconel Alloy 600. Special Metals, 2007. p. 16. (<http://www.specialmetals.com/documents/Inconel%20alloy%20600.pdf>)

47. Inconel Alloy 690. Special Metals, 2007. p. 8. (<http://www.specialmetals.com/documents/Inconel%20alloy%20690.pdf>)

48. Chang, H. C., and Grant, N. J. 1956. Mechanism of intercrystalline fracture. *Journal of Metals* 8 (AIME Trans. 206): 544-551.

49. Tegart, W. J. M. 1967. The role of ductility in hot working. *Ductility*, pp. 133-177. ASM International.

50. McQueen, H. J., and Jonas, J. J. 1975. Recovery and recrystallization during high temperature deformation. *Treatise on Materials Science and Technology* 6: 393-493.

51. Shapiro, E., and Dieter, G. E. 1970. High temperature-high strain rate fracture of Inconel

600. *Metallurgical Transactions* 1: 1711-1719.

52. Luton, M. J., Dorvel, R., and Petkovic, R. A. 1980. Interaction between deformation, recrystallization and precipitation in niobium steels. *Metallurgical Transactions A* 11A(3): 411-420.

53. Scriven, R. A., and Williams, H. D. 1965. The derivation of angular distributions of planes by sectioning methods. *Transactions of the American Institute of Mining, Metallurgical and Petroleum Engineers* 233(8): 1593-1602.

54. Garofalo, F. 1967. Ductility in creep. *Ductility*. Eds. ASM International, pp. 87-132.

55. Gandhi, C., and Raj, R. 1981. An upper bound on strain rate for wedge type fracture in nickel during creep. *Metallurgical Transactions A* 12A(3): 515-520.

56. Waddington, J. S. 1968. Conditions affecting the mechanism of fracture at high temperatures. *Philosophical Magazine* 17(145): 51-59.

57. Williams, J. A. 1969. General approach to creep failure resulting from wedge crack growth. *Philosophical Magazine* 20(165): 635-639.

58. Langdon, T. G. 2006. Grain boundary sliding revisited: Developments in sliding over four decades. *Journal of Materials Science* 41(3): 597-609.

59. Shapiro, E., and Dieter, G. E. 1971. Fracture and ductility in hot torsion of nickel. *Metallurgical Transactions* 2(5): 1385-1391.

60. Yeniscavich, W. A. 1966. Correlation of Ni-Cr-Fe alloy weld metal fissuring with hot ductility behavior. *Welding Journal* 45(8): 344-s to 356-s.

61. Humphreys, F. J., and Hatherly, M. 2004. *Recrystallization and Related Annealing Phenomena*. Oxford, Elsevier, 11-66.

62. Humphreys, F. J., and Hatherly, M. 2004. *Recrystallization and Related Annealing Phenomena*. Oxford, Elsevier, 215-266.

63. Humphreys, F. J., and Hatherly, M. 2004. *Recrystallization and Related Annealing Phenomena*. Oxford, Elsevier, 415-450.

64. Doherty, R. D., Hughes, D. A., Humphreys, F. J., Jonas, J. J., Jensen, D. J., Kassner, M. E., King, W. E., McNelley, T. R., McQueen, H. J., and Rollett, A. D. 1997. Current issues in recrystallization: A review. *Materials Science & Engineering A* A238(2): 219-274.

65. Suh, D. W., Cho, J. Y., and Nagai, K. 2004. Effect of initial grain size of austenite on hot-deformed structure of Ni-30Fe alloy. *Metallurgical and Materials Transactions A* 35A(11): 3399-3408.

66. Bruemmer, S. M., Charlot, L. A., and Henager Jr., C. H. 1988. Microstructure and microdeformation effects on intergranular stress corrosion cracking of Alloy 600 steam generator tubing. *Corrosion* 44(11): 782-788.

67. Bruemmer, S. M., and Henager Jr., C. H. 1986. High voltage electron microscopy observations of microdeformation in Alloy 600 tubing. *Scripta Metallurgica* 20(6): 909-914.

68. Luton, M. J., and Sellars, C. M. 1969. Dynamic recrystallization in nickel and nickel-iron alloys during high-temperature deformation. *Acta Metallurgica* 17(8): 1033-43.